

New insights on stress rotations from a forward regional model of the San Andreas fault system near its Big Bend in southern California

D. D. Fitzenz

U.S. Geological Survey, Menlo Park, California, USA

S. A. Miller

Institute of Geophysics, Swiss Federal Institute of Technology (ETHZ), Zürich, Switzerland

Received 12 November 2003; revised 6 April 2004; accepted 17 May 2004; published 11 August 2004.

[1] Understanding the stress field surrounding and driving active fault systems is an important component of mechanistic seismic hazard assessment. We develop and present results from a time-forward three-dimensional (3-D) model of the San Andreas fault system near its Big Bend in southern California. The model boundary conditions are assessed by comparing model and observed tectonic regimes. The model of earthquake generation along two fault segments is used to target measurable properties (e.g., stress orientations, heat flow) that may allow inferences on the stress state on the faults. It is a quasi-static model, where GPS-constrained tectonic loading drives faults modeled as mostly sealed viscoelastic bodies embedded in an elastic half-space subjected to compaction and shear creep. A transpressive tectonic regime develops southwest of the model bend as a result of the tectonic loading and migrates toward the bend because of fault slip. The strength of the model faults is assessed on the basis of stress orientations, stress drop, and overpressures, showing a departure in the behavior of 3-D finite faults compared to models of 1-D or homogeneous infinite faults. At a smaller scale, stress transfers from fault slip transiently induce significant perturbations in the local stress tensors (where the slip profile is very heterogeneous). These stress rotations disappear when subsequent model earthquakes smooth the slip profile. Maps of maximum absolute shear stress emphasize both that (1) future models should include a more continuous representation of the faults and (2) that hydrostatically pressured intact rock is very difficult to break when no material weakness is considered. *INDEX TERMS:* 8150

Tectonophysics: Plate boundary—general (3040); 8164 Tectonophysics: Stresses—crust and lithosphere; 8010 Structural Geology: Fractures and faults; 8045 Structural Geology: Role of fluids; 3210 Mathematical Geophysics: Modeling; *KEYWORDS:* fault strength, stress orientations, numerical modeling

Citation: Fitzenz, D. D., and S. A. Miller (2004), New insights on stress rotations from a forward regional model of the San Andreas fault system near its Big Bend in southern California, *J. Geophys. Res.*, 109, B08404, doi:10.1029/2003JB002890.

1. Introduction

[2] Plate boundaries are zones of complex deformation over widths of tens or hundreds of kilometers and may contain multiple tectonic regimes. Insight into the forces (e.g., stresses) acting on these fault systems is therefore essential to understanding the mechanics of their deformation. Spatial patterns and temporal evolution of both stress orientation and absolute magnitude are needed to determine what complexity in the stress orientations results from the boundary conditions and geometry alone and how the fault behavior feeds back on the stress distribution. That is, when, how, and for how long the seismic behavior on the faults perturbs the surrounding stress patterns. A better understanding

of these two classes of stress analysis would lead to more insight into two much debated issues: the validity of the hypotheses for the inversion of focal mechanisms to infer stress orientations (e.g., the assumption of relatively homogeneous stress over space and time [Michael, 1987]), and the link between the strength of the faults and the orientation of the maximum stresses with respect to their strike. Borehole measurements can provide information on the subsurface stress state [Brereton and Muller, 1991; Zoback and Healy, 1992; Tsukahara et al., 1996; Ikeda et al., 2001], and stress orientations at seismogenic depths can be determined from earthquake focal mechanisms [Hardebeck and Hauksson, 1999, 2001; Provost and Houston, 2001; Townend and Zoback, 2001]. However, no direct evaluation of absolute stress values is possible in the 5–20 km depth interval containing the hypocenters of most earthquakes.

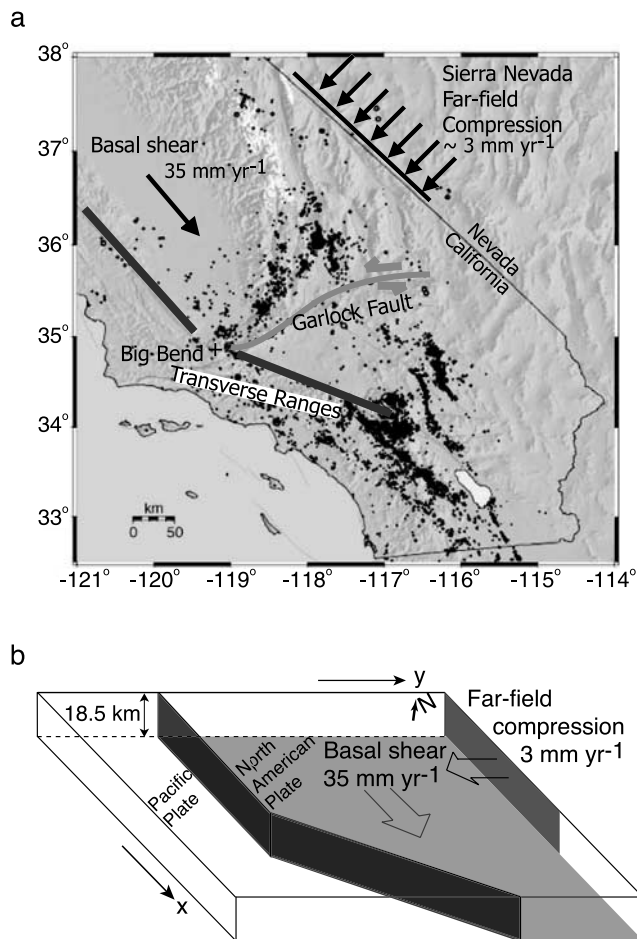


Figure 1. (a) Seismotectonic map of southern California showing the major fault traces (thin lines) and the seismicity between October 2000 and September 2001 (recorded by SCSN/TriNet). The black arrows show the boundary conditions for our model. The thick gray lines show the two segments of the San Andreas fault included in our simulations. (b) Three-dimensional block diagram of the initial model (no fault).

[3] In the present modeling study we focus on a strike-slip plate boundary with a convergent component to better constrain the state of stress along the San Andreas fault (SAF). To provide a testable system, we chose the simplified geometry of the Big Bend in the San Andreas fault in southern California. The purpose of this paper is twofold. First, we develop a tectonic-scale model of the southern SAF system to investigate boundary conditions that result in the development of the observed stress, and subsequent tectonic regimes. Second, once the boundary conditions are determined, we investigate the long-term slip behavior along two major strike-slip fault segments representing the SAF north and south of its Big Bend. We determine subsequent optimal orientations for faulting in the region and the effects of the fault system behavior on stress orientations as well as the conditions required to break intact rock. The model simulations assume a system where fresh fractures develop in response to the applied boundary conditions in an intact crust under hydrostatic fluid pressure.

The faults that develop then assume properties of a frictional interface, with a lower friction coefficient. After sufficient slip has accumulated along these strong faults, ductile creep and compaction are incorporated to model low-permeability fault zones that develop along high-slip fault zones [Faulkner and Rutter, 2001]. These mature viscoelastic fault zones differ from the initial fault in that they tend to weaken with time [Fitzenz and Miller, 2003], therefore allowing a comparison of the stress orientation results obtained for different model fault fluid pressures.

2. Tectonic Setup and Test of the Boundary Conditions

[4] The San Andreas fault system is 1300 km long. In this study we model the portion of this system centered at a location south of the Carrizo plains called the Big Bend because there the fault exhibits a large change in strike. The creeping section of the SAF is north of our model region, and its behavior is not discussed in the present study.

[5] Since our aim will be to study the behavior of the fault system itself, we chose the simplest boundary conditions that produce tectonic domains close to those observed in the modeled area. The model plate boundary has the simplified geometry of the SAF, and the thickness of the seismogenic layer is 18.5 km (i.e., the focal depths of most earthquakes in southern California in the 1991–1999 time period are within the 0–18 km interval, with a number of focal depth below 15 km [Zhu and Helmberger, 1996]). The tectonic loading is decomposed into two main components (Figure 1b). First, the tectonic shear loading is applied as a dislocation on a horizontal plane at the base of the model North American plate (at 18.5 km depth) and is parallel to the plate boundary north of the Big Bend (i.e., the Pacific plate is fixed). The plate velocity is 35 mm yr⁻¹. Second, the east-west compression north of the bend (due to motion of the Sierra Nevada block) is approximated by a vertical dislocation surface parallel to the northern strike of the plate boundary and applied at the far-field boundary (at 400 km east of the plate boundary). It results in fault-normal compression rates of ~3 mm yr⁻¹ [Argus and Gordon, 1991; Prescott et al., 2001]. South of the bend, the Mojave block does not show such an east-west motion (see the crustal velocity map version 3 issued by the Southern California Earthquake Center (Z.-K. Shen et al., The SCEC crustal motion map, version 3.0, 2003, available at <http://epicenter.usc.edu/cmm3/>)).

[6] To test the model boundary conditions, we apply a displacement on the model boundaries corresponding to 100,000 years of tectonic loading, and we compare calculated and observed tectonic regimes. Because we consider a linear elastic half-space, t years of tectonic loading at a velocity V expressed in mm yr⁻¹ is equivalent to a unique displacement of $V \times t$ mm.

[7] Using an approach similar to that of Simpson [1997], we use the magnitude and orientation of the principal stresses to infer tectonic regimes in a crust with no preexisting faults. The stress tensor is calculated on a horizontal grid at midseismogenic depth (8.5 km) by applying the analytical solution of Okada [1985] to the two basal and far-field dislocation planes undergoing a slip of 100,000 years times the GPS-constrained slip rates. We add the isotropic

Table 1. The Nine End-member Tectonic Regimes

Vertical Principal Stress σ_v	$R = 0$ ($\sigma_2 = \sigma_3$)	$R = 0.5$ ($\sigma_2 = (\sigma_1 + \sigma_3)/2$)	$R = 1$ ($\sigma_1 = \sigma_2$)
$\sigma_v = \sigma_3$	reverse strike slip	pure reverse	constrictive
$\sigma_v = \sigma_1$	radial extensive	pure normal	normal strike slip
$\sigma_v = \sigma_2$	reverse strike slip	pure strike slip	normal strike slip

lithostatic stress (the overburden) by assuming a homogeneous rock density of 2700 kg m^{-3} and a flat topography. The calculated tectonic regime at a given location on the grid is obtained by combining the vertical principal stress and the ratio $R = (\sigma_2 - \sigma_3)/(\sigma_1 - \sigma_3)$, where σ_1 , σ_2 , and σ_3 are the principal stresses. The R ratio takes values continuously between 0 and 1. We identify characteristic tectonic domains corresponding to $R \sim 0$, $R \sim 0.5$, and $R \sim 1$ for each vertical principal stress (i.e., end-member cases, also presented in Table 1). Throughout the paper, when discussing map views of the model area, the x axis is parallel to the plate boundary north of the bend and $x = 0$ at the bend, whereas the y axis points to the east and $y = 0$ along the plate boundary north of the bend.

[8] Figure 2 shows that the plate boundary lies in a strike-slip regime, while compressive to transpressive regimes develop west of the southern part of the plate boundary (for $x > 0$), reminiscent of the Transverse Ranges (see Figure 1a). A large area east of the plate boundary (for $x > 0$) also exhibits a transpressive regime. However, since we did not include the specific boundary conditions to account for the presence of the East California Shear Zone, we will not discuss this last feature.

[9] The Coulomb failure stress is defined as $\text{CFS} = \tau - \mu \times \sigma_{\text{eff}} - c$, where τ and σ_{eff} are the shear and effective normal stress acting on defined planes and c is cohesion. We use this failure criterion to identify where faults would develop in the model region in response to the chosen boundary conditions. The initial strength of the model is assumed to be that of intact rock, with a high friction coefficient ($\mu = 0.9$), an assumed cohesion of $c = 20 \text{ MPa}$, and hydrostatic pore pressure [Townend and Zoback, 2000]. Figure 3 shows a map of CFS calculated on optimally oriented planes for new fractures at

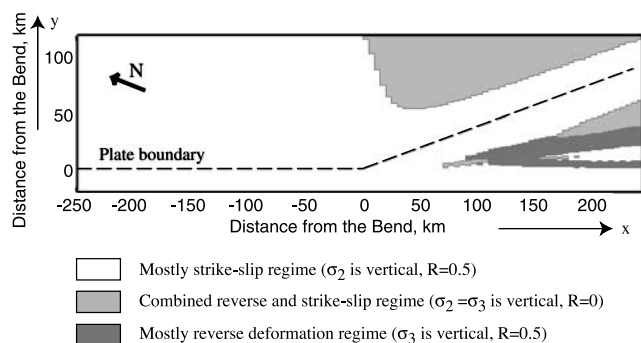


Figure 2. Main tectonic domains calculated from the stress tensor at 8.5 km depth for 100,000 years of basal shear drag and far-field compression. The plate boundary lies in a strike-slip regime, while transpression is shown to develop southwest of the bend (e.g., transverse ranges). The coordinates are centered at the bend.

8.5 km depth (see section 5.3 for the details of the three-dimensional (3-D) calculation of optimal orientation for faulting). White corresponds to $\text{CFS} \sim 0$. A narrow region along the plate boundary is shown to be the first area to accumulate enough stress to reach the failure criterion. In particular, the high values of CFS (up to 400 MPa) north of the bend show that a fault would be created there well before 100,000 years of plate motion. The plate boundary region south of the bend, being oblique to the major plate motion direction, develops very high normal stresses that inhibit this part of the plate boundary from breaking as early as its northern counterpart, despite shear stresses of the same order of magnitude. Indeed, the shear stress loading rate on the southern plate boundary is $\sim 94\%$ of that on the northern part (i.e., same source of deviatoric stress as for the northern region but resolved on a plane striking at 20° to the direction of shear loading). However, if the northern part failed in earthquakes, stress transfer from this slip would be likely to load the southern part to failure.

3. Fault Models

[10] The evolved stress state developed during the initial loading phase was shown to be consistent with creating a fault segment north of the bend and initiating the creation of another one south of the bend. Therefore the model fault system includes two 200 km long right-lateral strike-slip fault segments, discretized into subfaults, with a change in strike of 20° . The two fault segments are separated by a region of intact rock as explained below and shown on Figure 1.

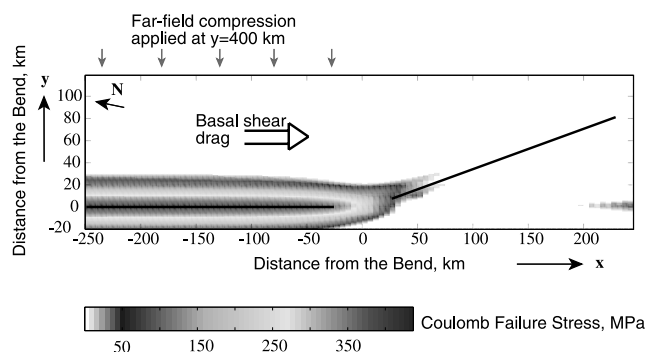


Figure 3. Map of Coulomb failure stress (CFS) calculated at 8.5 km depth due to 100,000 years of tectonic loading. The two modeled fault segments of the San Andreas fault (black lines) are shown to be the first faults to accumulate enough stresses to reach the failure criterion. The southern segment accumulates less CFS because of the high normal stresses. White corresponds to $\text{CFS} \ll 15 \text{ MPa}$. See color version of this figure at back of this issue.

[11] The reason behind the choice of an intact Big Bend region between the two prescribed fault segments is two-fold. Numerically, this prevents the occurrence of any singularity in stresses that might result from slip on dislocations intersecting at an angle (from the two fault segments and the basal dislocation). It also provides an interesting test of what it would take to break a long-locked, lithified fault segment located between two active fault segments. Although not an appropriate description of the San Andreas fault at this location, this geometry allows us to test in a generic way what it would take to link up two active fault segments separated by intact or lithified rock. Therefore, even though this (initial) geometry does not reflect the present-day Big Bend tectonics, its evolution with time in the model has interesting general implications for the strength of the crust (i.e., for other fault systems).

[12] We do not model the complex process of fracture nucleation and growth, and instead, we simplify the problem by assuming that the fracturing associated with the creation of the model faults reduces their frictional resistance to that of a sliding interface (e.g., $\mu = 0.6$) with zero cohesion, and that it reduces significantly the shear stress on the faults, so that zero initial shear stress is prescribed on the model faults for simplicity. A direct drawback of this approach is the lack of information on the state of stress in the crust surrounding the faults at $t = 0$ in the simulation. We saw on Figure 3 that the Coulomb Failure Stress was highly localized in a narrow (40 km, or twice the depth at which the basal shear drag is applied) band centered on the faults, showing that even in 100,000 years, the stress accumulation is not large enough to break intact rock at a distance greater than 20 km from the plate boundary (see discussion in section 7). In the long-term simulation, at $t = 0$, the crust is initially submitted to the lithostatic stress only and the shear stress builds up as the result of tectonic loading, for $t > 0$. The limitations of this assumption are discussed in each result section. Fault slip and its effect on the surrounding stress state is investigated over an ≈ 4000 year interval. The details of the time evolution of the model faults properties are given and discussed in section 4.

[13] An improvement to the model would be to impose the fault geometry of the two SAF segments while ascribing the properties of intact rock to each subfault (e.g., high friction and nonzero cohesion) to monitor the time to the fracture, reducing the subfault properties to those of a frictional interface only once the initial failure has occurred. This would allow the stresses developed from plate motion to be maintained in the crust in a more accurate way provided a detailed handling of stress transfer associated with fracturing was incorporated. Other types of boundary conditions could also be tested.

3.1. Initial Fault Model

[14] The two SAF fault segments are discretized into subfaults measuring 2.0 km along strike by 0.5 km down-dip. The state of each cell is monitored during model simulations, and subfault properties include shear and normal stresses, porosity, pore pressure, fault zone width, and Skempton's coefficient. The model includes stress transfer between cells, undrained poroelastic effects, and coseismic pore pressure redistribution. The reader is referred to *Fitzenz and Miller* [2001] for a full description

of the model and a discussion of the model assumptions and parameters.

[15] For completeness, the following sections, and corresponding appendices, present a summary of the main features of the modeling.

3.1.1. Elasticity and Poroelasticity

[16] In our model, faults are idealized by a displacement discontinuity (i.e., dislocation) across a surface (i.e., dislocation plane). Therefore seismic slip on a fault plane is modeled as a slip vector acting on a dislocation plane.

[17] To calculate strain changes due to displacements (either interseismic at the boundaries of the model, i.e., tectonic loading, or coseismic on the subfaults), we use the analytical solution derived by 1992 [*Okada*, 1985]. We then calculate the resulting stresses with Hooke's law. The elastic moduli (compressibility and rigidity) are equal to 30 GPa.

[18] The mechanical behavior in rocks subjected to changes in either confining pressure or pore fluid pressure has commonly been cast in terms of the effective stress relationship [*Terzaghi*, 1923; *Hubbert and Rubey*, 1959], where the effective stress σ_{eff} is given by

$$\sigma_{\text{eff}} = \sigma_n - P_f, \quad (1)$$

where σ_n is the normal stress acting on a frictional surface and P_f is the pore pressure. Although this relationship can be used to calculate the strength at failure, it does not always represent the poroelastic loading properly. It appears to be valid in many porous permeable rocks; however, a more general expression for the static case is $\sigma_{\text{eff}} = \sigma_n - \alpha P_f$ [*Nur and Byerlee*, 1971], where α is a poroelastic constant found empirically and can range from 0 to 1.0 for fractured and intact rocks. Measured values of α depend on the mineralogy of the sample and whether it is drained or undrained [*Morrow et al.*, 1994]. *Lockner and Beeler* [2003] also showed that α varies with effective confining pressure for sandstones. Although these deviations from equation (1) might be large depending on the geology and the processes of the fault zones, their study is beyond the scope of the present work, and $\alpha = 1$ is assumed throughout. Pore pressures increase because of a change in the mean confining pressure from a poroelastic effect approximated by

$$\Delta P_f|_{\text{no flow}} = B \frac{\text{Tr}(\Delta\sigma)}{3}, \quad (2)$$

where $\text{Tr}(\Delta\sigma)$ is the trace of the tensor of stress changes (positive in compression) and B is Skempton's coefficient. Equation (2) is applied in undrained conditions (no flow) on the cells of homogeneous pore pressure composing the model fault segments. Few values of Skempton's coefficient have been measured in fault zones. We chose $B = 0.6$ [*Talwani et al.*, 1999].

3.1.2. Hydraulic Properties of the Model Faults

[19] Interseismic pore pressure increases are allowed independently in each subfault by assuming an interseismic compaction rate, randomly distributed around $3 \times 10^{-6} \text{ yr}^{-1}$ and ranging between $9 \times 10^{-7} \text{ yr}^{-1}$ and $5 \times 10^{-6} \text{ yr}^{-1}$. The hydraulic properties of the slipping region are assumed to change dramatically during the seismic event, resulting in a much greater hydraulic connectivity and subsequent fast pore pressure equilibration within the slipped patch

[Sibson, 1992; Miller *et al.*, 1996]. The random compaction rate along the fault is the only imposed source of initial heterogeneity. Potentially important sources of pore pressure increase that we do not consider include a fluid source at depth [Rice, 1992; Gratier *et al.*, 2003] and frictional heating [Andrews, 2002]. In contrast to Fitzenz and Miller [2001], who completely sealed off subfaults from each other, the subfaults now have a defined interseismic permeability. No flow is allowed out of the fault zone. The interseismic permeabilities of the model subfaults are computed as stated in Appendix A and range from $\sim 10^{-21}$ to $\sim 10^{-19}$ m², depending on the evolving porosity. These values are used in a finite difference algorithm to calculate in-plane interseismic diffusion.

[20] Coseismic porosity production is modeled by frictional dilatancy and is assumed to be proportional to slip. Porosity production follows the model of Sleep [1995]:

$$\frac{\partial \phi}{\partial \delta} = \frac{\beta_m (\phi_m - \phi) \tau}{W \phi_m \sigma_n}, \quad (3)$$

where ϕ is the porosity created with slip δ , β_m is the fraction of energy that goes into the new crack creation, ϕ_m is the saturation porosity which limits the amount of crack porosity that can be generated (i.e., $\phi < \phi_m$), τ and σ_n are the shear and normal stress acting on the slipped cell, and W is the fault zone width. The values for β_m , ϕ_m , and W were taken from Sleep [1995]. The porosity change is used to update the storage capacity ($(\beta_\phi + \beta_f)\phi$, i.e., pore and fluid compressibility times porosity) of the cells just before the redistribution of pore pressure. In addition, this coseismic change in the porosity of slipped cells yield interseismic pore pressure increase rates that vary with time via

$$\frac{\partial P_f}{\partial t} = \frac{-\dot{\phi}}{\phi(\beta_\phi + \beta_f)}. \quad (4)$$

3.1.3. Earthquake Generation and Propagation

[21] The failure stress is the Coulomb failure stress that explicitly includes the pore pressure state. The initial static friction coefficient (μ_s) is taken as constant and uniform over the fault planes and is assumed to be 0.6. We treat the case in which strength heterogeneity only comes from variations in pore pressure. The quasi-static treatment of the modeling ensures that one cell reaches the failure criterion at the beginning of each time step. Slip on that cell is calculated to correspond to an assumed stress drop (a percentage of the prefailure shear stress, here chosen at 25%). See Miller *et al.* [1999] for a discussion of the influence of this assumption on the overall fault behavior. Quasi-static, instantaneous stress transfer from the failure of this cell (still in undrained conditions) can initiate failure of other cells, and the model is then cycled until all cells are below the failure condition. When the system is stable with respect to the stress state, pore pressures are redistributed within the slipped patches and may induce additional failures. If so, the algorithm returns to the “undrained rupture” loop just described. This sequence is then cycled until the system is in equilibrium. These (quasi-static) rupture loops ignore wave propagation but provide insight into the propagation of the ruptures and coseismic stress transfers. The

total slip on all subfaults of a fault segment during a given time step is used to calculate first the scalar seismic moment of the event and then its magnitude.

[22] Note that when slip occurs on a cell, its friction reduces to a dynamic value ($\mu_d = 0.5$) for the duration of that event. This switch approximates a slip-weakening model for friction and is discussed by Miller [2002]. After the event, friction is reset to the static value because computing a time-dependent strength recovery would add another level of iteration when determining the time step necessary to initiate one hypocenter (e.g., rigorously quasi-static). Note also that although both the compaction rates and individual stress drops are arbitrary, Miller *et al.* [1999] showed that changing these values does not change the overall behavior of the fault. Fitzenz and Miller [2001] also showed that although cells of higher compaction rates are more likely to be hypocenters, the final size of the event is independent of this arbitrary random distribution but depends mostly on the level of organization of the stress state on the fault plane at a given time.

3.2. Time-Dependent Compaction and Shear Creep

[23] After model conditioning, i.e., once a stress state is reached on the faults that allows for the propagation of the first large ruptures, the fault properties are those of a ductile fault core, hydraulically disconnected from the surrounding rocks by a quasi-impermeable narrow seal. A small diffusive leakage out of the fault zone during interseismic periods is allowed. Ductile compaction depends on effective stress and a porosity-dependent “bulk” viscosity term, and shear creep varies with shear stress, fault zone width, and a porosity-dependent shear viscosity term as described by Fitzenz and Miller [2003] and as summarized in Appendix B for the reader’s convenience. Ideally, creep compaction should depend on porosity, effective confining stress, differential stress, temperature, rock type, grain-size distribution, and the nature of the pore fluid, but no such model is currently available.

4. Evolved Stress State and Seismicity on the Model Faults

[24] In order to understand the time evolution of the tectonics of the (model) region (as discussed in section 5) it is important to study both the stress and pore pressure evolution in the prescribed faults and the generated synthetic seismicity. Figures 4 and 5 show the time evolution of the stress state on both the northern and the southern fault segments, respectively. Each point of these curves represents the property averaged over the whole fault plane (both in depth and along strike). The seismicity time lines and statistics are shown on Figure 6. The three main phases in the model fault history are (1) a continuous stress buildup for the first ~ 1800 years due to plate motion loading; (2) the readjustment and self-organization of the stress state, evidenced by the occurrence of the first large ruptures (until $t \sim 3000$ years), and (3) fault weakening due to the onset of ductile compaction.

4.1. Phases 1 and 2

[25] On the northern fault the first phase is characterized by a steady increase in shear stress τ from tectonic loading

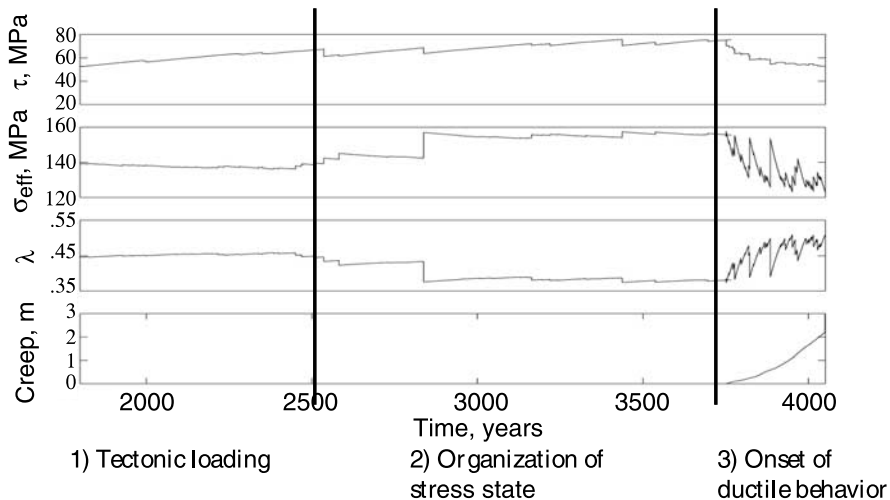


Figure 4. Time evolution of the properties on the northern segment averaged over the whole plane. Top to bottom panels are for shear stress, effective stress, the degree of overpressure λ , and the amount of creep slip. The first part ($t = 0$ to $t \sim 2500$ years) is the stress buildup phase. The first large events occur for $t > 2800$ years and induce large drops in pore pressure. Creep slip and ductile compaction initiate at $t = 3750$ years.

and a slight decrease in effective stress σ_{eff} due to pore compaction (Figure 4). Fault overpressure is described by the factor $\lambda = P_f/\sigma_n$, where P_f and σ_n are pore pressure and normal stress, respectively. On the southern fault, λ and σ_{eff} appear constant because of the oblique orientation of the fault with respect to the basal shear drag. In this case, pore pressure increases from compaction are counterbalanced by the increase in tectonic normal stress. The seismicity (Figure 6) is low on both faults during this first phase. The second phase shows an increase in seismicity and the first large events ($M_w > 7$) occur at $t \sim 2500$ years and $t \sim 3000$ years on the northern and the southern segments,

respectively. The fact that the northern segment fails first is related to its lower initial frictional strength (e.g., lower normal stress buildup rate than that of the southern segment).

4.2. Phase 3

[26] At $t = 3750$ years, when phase 2 is stopped, both faults sustain high shear stresses (i.e., strong faults). Shear creep and ductile compaction are introduced. The high effective stresses lead to pore pressure increase rates (Appendix B, equation (B1)) much larger than the shear stress increase rate, promoted by tectonic loading but reduced by shear creep. The combined effects of shear

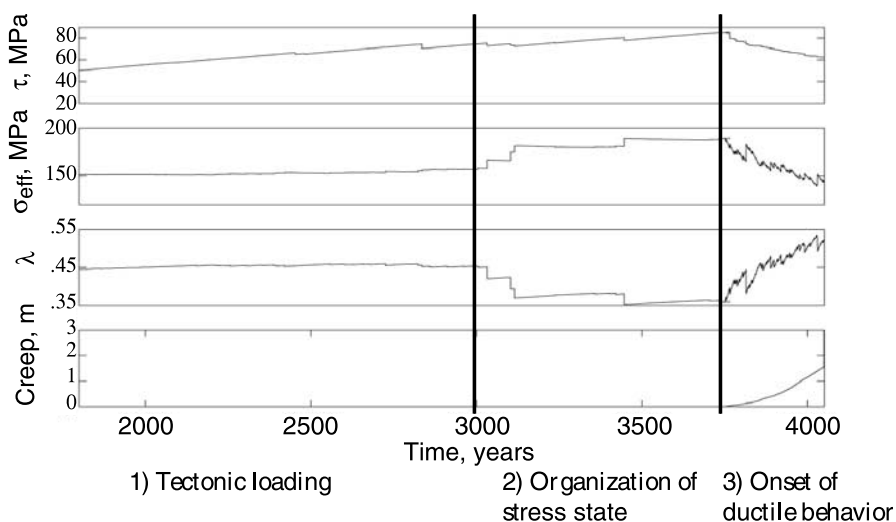


Figure 5. Time evolution of the properties on the southern segment averaged over the whole plane. Same as Figure 4. Because of the 20° angle between the fault strike and plate motion the normal stress buildup rate is larger than in the previous case, initially leading to a stronger fault. As ductile compaction initiates, it leads to a larger compaction rate and faster overpressurization of the fault. The average amount of creep is $2/3$ the creep slip on the northern fault.

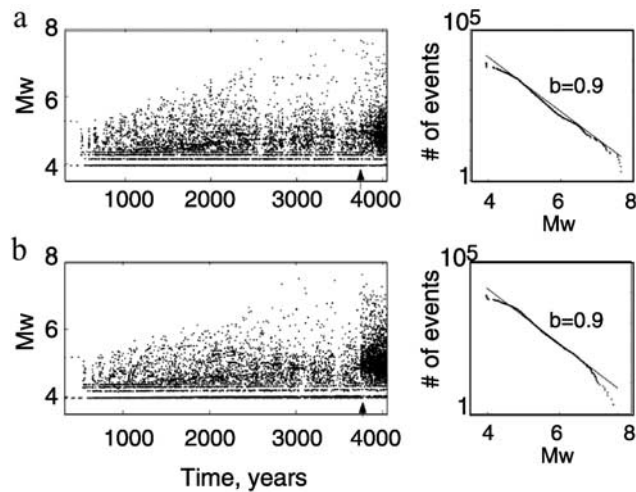


Figure 6. Seismicity time lines and frequency-magnitude statistics (a) for the northern strike slip fault segment and (b) for the southern segment. The arrows show the onset of shear creep and ductile compaction at $t = 3750$ years. The density of the seismicity reflects the strength of the faults shown in Figures 4 and 5. Both faults exhibit Gutenberg-Richter laws with a b value of 0.9 (shown by the straight line).

creep and compaction lead to fault weakening. During this phase the density of medium size events ($4.5 < M_w < 6$) increases dramatically, very rapidly on the southern segment and more progressively on the northern segment (Figure 6). On the northern fault segment, large events reaching the surface allow for large pore pressure drops, resulting in a fault behavior comparable to that obtained in the 1-D fault model of *Sleep and Blanpied* [1992]. Large pore pressure drops are observed when ruptures reach the surface and are controlled by the hydrostatic boundary condition. When the ruptures do not reach the surface, fluids can not be expelled, overpressures are maintained, and the fault evolves to a weak fault (i.e., the fault can not sustain high shear stresses).

[27] The fact that the value of λ averaged over the fault planes is ~ 0.55 on both faults at the end of the simulation should not hide the fact that it locally reaches values as high as 0.60 on the northern fault and 0.70 to 0.75 on the southern fault, at depths between 6 and 18 km.

[28] Note that the creep rate (averaged over the fault plane) on the northern fault segment (7.6 mm yr^{-1}) is greater than on the southern one (5 mm yr^{-1}). Indeed, both shear stress and fault zone width are larger on the northern segment because during phase 3 the fault is stronger (i.e., can sustain higher shear stresses) and undergoes larger slip at depth (see Appendix B, equation (B2)). For these reasons, creep slip is maximum at depth, and at 18 km depth the accumulated creep slip over 300 years yields average creep rates on the order of plate velocity.

[29] For interest, we monitored the stress and pore pressure state on a blind dipping fault oriented 25° to the northern fault between $x = -200$ and $x = -109$ km to mimic the fold and thrust belt subparallel to the southern part of the central SAF. The stress state shows very low stresses and that incipient faulting would be a late time feature. As a reminder, the northern model fault is only

200 km long and therefore does not encompass the creeping segment of the SAF.

5. Resulting Regional Tectonic Evolution

[30] In this section we explore the spatial and temporal stress orientation patterns to address some important issues about interpreting stress orientations around active fault zones. The first step is to be able to determine what level of complexity in the stress orientations results from the boundary conditions and geometry alone. The second is to determine how the fault behavior feeds back on the stress distribution. That is, when, how, and for how long the seismic behavior on the faults perturbs the surrounding stress patterns, and how the orientation of the maximum compressive stresses relates to fault strength.

[31] *Rice* [1992] showed theoretically how stresses can rotate from high angles outside of the fault zone to low ($\sim 30\text{--}40^\circ$) within the fault zone due to high pore pressure in a fault zone that undergoes some plastic deformation. However, what controls the spatial and temporal patterns of stress orientations surrounding 3-D fault surfaces undergoing heterogeneous, not elliptical slip distributions, is still an open question.

[32] Our approach is to study the stress state evolution in the framework of the regional model. Section 2 described the effects of the loading boundary conditions and the geometry of the plate boundary alone in terms of tectonic regimes (or stress state) in the absence of faults. It shows a great spatial differentiation between areas in pure strike-slip regime and areas in transpressive to compressive regimes, on both sides of the southern part of the plate boundary.

[33] A comparison of these patterns with those obtained after several thousands of years of synthetic seismicity as well as large-scale tectonic loading show both large-scale and small-scale differences. We interpret them in terms of the cumulative right-lateral fault slip, seismic slip and overpressure profiles at the depth of the calculation, and the frequency-size statistics of the model earthquakes.

5.1. Tectonic Regimes

[34] We compare Figure 2 with the map of tectonic regimes calculated after 4000 years of fault model simulation to evaluate the feedback of fault behavior on the local to regional stress state. Figure 7 shows that the transpressive tectonic regime that developed both southwest and southeast of the model Big Bend as a result of the loading boundary conditions (Figure 2) now migrates north toward the bend because of the 4000 years of evolution of the stress state and the seismicity on the two model faults. The pattern mostly reflects the fact that both model faults are of finite length and right lateral (i.e., fault motion generates quadrants of compression and dilation). With accumulated right lateral slip the corresponding areas of increased compression merge and progressively change the local tectonic regime from strike slip to transpressive. Note that the extensional area southwest of the southern fault (black) is probably an artifact of the (coarse) discretization of the model basal loading dislocation. Similar extensional patches are already present in the model with no fault (as in section 2) when tectonic regimes are calculated at greater depth (e.g., 15 km, not shown here). This will be addressed

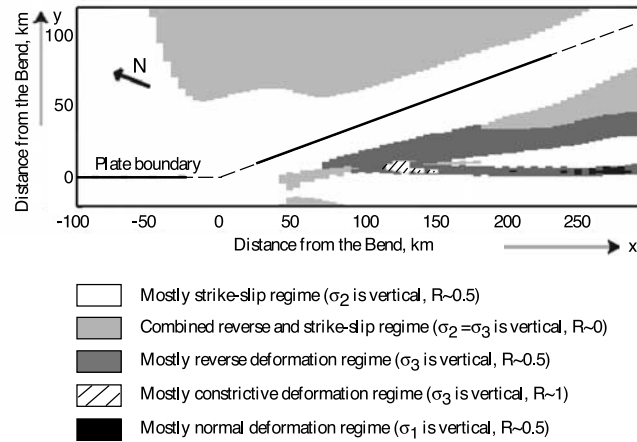


Figure 7. Map of evolved tectonic regimes, resulting from ~ 4000 years of plate motion and model seismicity, calculated at midseismogenic depth. Compare to Figure 2 to notice the similarities and the differences in the patterns due to fault slip.

in future studies where a triangular dislocation surface will replace the set of rectangular dislocations now used.

5.2. Stress Buildup in the Model Region and Stress Orientations

[35] Figure 8 shows the accumulated shear stress in the model due to the combined effect of plate motion and fault ruptures. This property is quantified by the maximum shear stress, i.e., $\tau_{\max} = (\sigma_1 - \sigma_3)/2$, and it is a useful measure since no assumption on (fault plane) orientations is needed.

[36] Although the level of shear stress decreases rapidly with distance from the plate boundary, stress transfer from previous earthquakes, as well as the overall slip deficit, locally maintain a high maximum shear stress near the faults (up to 70 MPa). Low values close to the faults reflect the stress drops associated with large earthquakes, and the heterogeneity of the stress field along the faults reflects the heterogeneity in slip (see discussion below). Exceptionally high values are reached at the terminations of the faults, in particular at the bend in the plate boundary (with values up to 120 MPa). The isolated red points show singularities in the stress field at the tips of a dislocation, i.e., the grid point is very close to the boundary of a slipping cell. At distances greater than about 50 km from the faults the level of shear stress is extremely low, showing that 4000 years of tectonic loading are not enough to critically stress the crust surrounding the model plate boundary, namely, because of the stabilizing effect of earthquakes. A more consistent approach would be to add the level of stress in the crust present at the creation of the two faults. Even though the level of stress might then be larger close to the plate boundary, it is not likely to be the case far from it.

[37] The maximum horizontal stress $\sigma_{H\max}$ is computed at 8.5 km depth. It is compressive in most of the model region. Figure 8b shows the orientation of $\sigma_{H\max}$ with respect to the x axis (strike of the northern segment). Stress $\sigma_{H\max}$ is consistently oriented $\sim 45^\circ$ to the northern segment, and $\sim 55^\circ$ to the southern segment in a 20 km wide band. There is a gradient from the far-field angles ($y > 0$) down to the near fault values (approximately from -45° to -35° for the northern segment in the y direction and from -60° to -40°

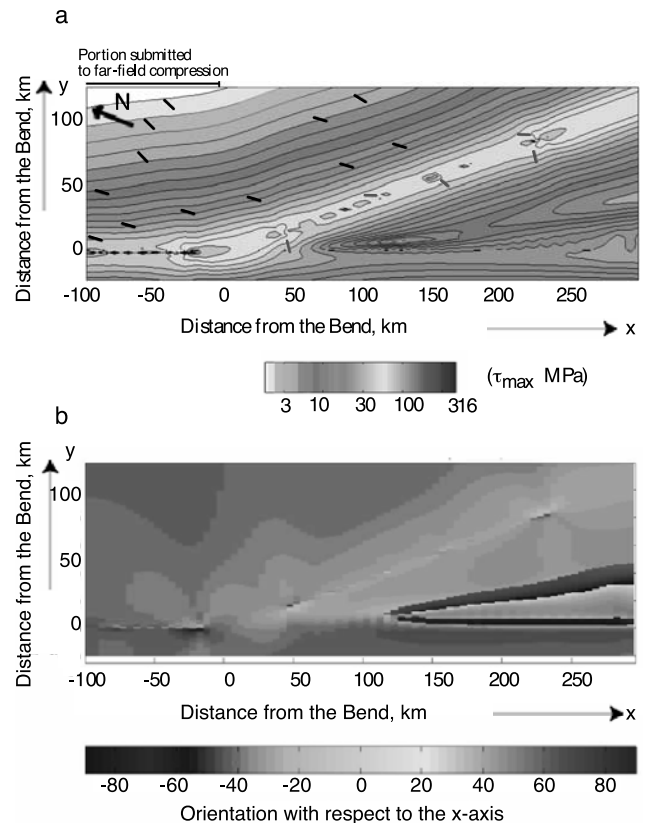


Figure 8. (a) Maximum shear stress (colors) and $\sigma_{H\max}$ orientations (characteristic trends, white lines, and local perturbations, red lines) and (b) orientation of $\sigma_{H\max}$ relative to x axis. Both maps are calculated at 8.5 km depth. τ_{\max} is maximum in a 40 km wide zone (~ 70 MPa) centered at the plate boundary and is largely perturbed near the faults (e.g., stress drops and stress transfer). The term σ_1 is consistently oriented $\sim 45^\circ$ to the northern segment, and $\sim 55^\circ$ to the southern segment in a 20 km wide band. However, it locally rotates to be either almost perpendicular or subparallel to the fault strike. See color version of this figure at back of this issue.

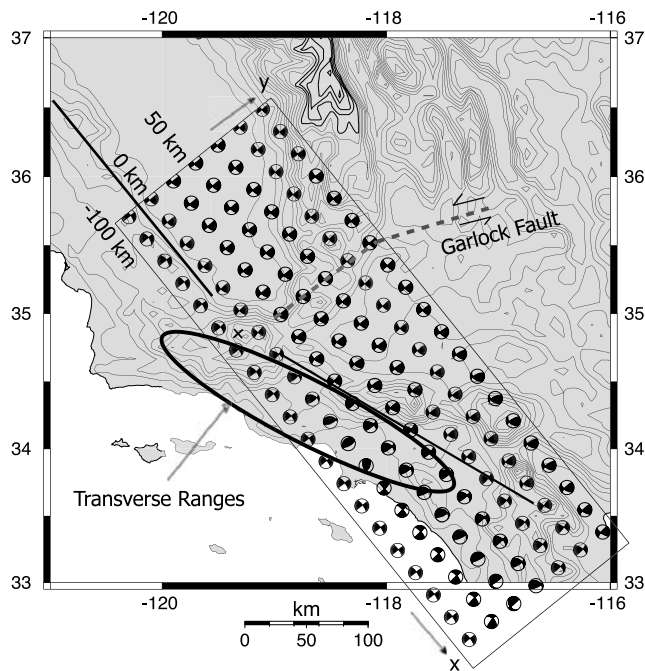


Figure 9. “Beach balls” calculated $t = 4050$ years at 8.5 km depth superposed onto the topography map of southern California (made with the Online Map Creation (OMC) tool of M. Weinelt, available at <http://www.aquarius.geomar.de/>, accessed at 5 April 2004). Most subvertical strike-slip faults parallel to the fault segments are right-lateral east of the plate boundary, whereas the ones perpendicular to the two segments are left lateral, with an orientation analogous to that of the Garlock fault (shaded area) just east of the bend. The faults that would develop in the model west of the bend have a strong reverse component, analogous to the Transverse Ranges.

for the southern segment, in the direction perpendicular to the fault strike, far field to near field). This gradient comes from the far-field compression boundary condition applied for $x < 0$ (north of the bend), the only source of deviatoric stress at distances greater than the width of the seismogenic layer. Since there is initially no model (thrust) fault capable of dissipating this accumulating fault-normal stress buildup the way the vertical strike-slip fault relieves the shear stress due to the basal shear drag, it is expected that the orientation of the maximum horizontal stress should be at higher angles in the model if the initial stress state in the crust was that prevailing at the creation of the faults. It should also rotate clockwise with time to reach values comparable to that observed ($\sim 70^\circ$) far from the SAF, as long as no reverse fault is created to accommodate this compression, especially if the San Andreas fault was modeled as a continuous fault across the bend.

[38] Even though the orientation of σ_{Hmax} is generally smooth around the model faults, it locally rotates to be either almost perpendicular or subparallel to the fault strike near the southern fault in a few places. A comparison with the slip profile at that depth shows a strong correlation between the heterogeneities in slip along strike and these rotations (see section 6). No such perturbation is observed on other parts of the faults where the slip profile is smooth,

suggesting that the stress rotations are an ephemeral result of local seismicity. In the triangular area southwest of the bend where the tectonic regime is compressive to transpressive, the maximum stress is oriented -70° to the x axis (e.g., roughly perpendicular to the plate boundary).

5.3. Optimal Orientations for Faulting

[39] Figure 8 shows that no significant off-fault shear stress has accumulated at this time in the model. In addition, no new fault would be created at the bend of the plate boundary in the model despite significant (>100 MPa) shear stress accumulation. This high crustal strength results from the chosen friction coefficient for intact rock (0.8 to 0.9) and the assumption that the crust is hydrostatically pressurized and it prevents CFS from becoming positive. Other assumptions, such as material weaknesses (e.g., lithology contrasts or flaws, preexisting faults or fractures, or high pore fluid pressures) might have to be invoked to reach a critical stress state in the model crust [Townend and Zoback, 2000]. As previously stated, we do not use the consequences of the initial model geometry to make any conclusion regarding the Big Bend in the San Andreas fault but rather use this “numerical experiment” to study the conditions needed to link two active fault segments in general.

[40] Nevertheless, we can investigate how this two-fault system would evolve with time and with what orientations new faults would be created in the tectonic regimes described above.

[41] A detailed description of the method used to calculate the optimal orientation (strike and dip) for faulting from a full 3-D stress tensor is given by Guéguen and Palciauskas [1992] and is summarized in Appendix C. For simplicity, we chose to represent a map of “beach balls” instead of the map of the two calculated sets of strike and dip angles, which are more difficult to visualize. The two possible nodal planes were calculated from the full stress tensor resulting from both plate motion and fault slip and approximated the two sets of optimal orientations for failure. The optimal nodal planes at $t = 4050$ years already satisfy the condition for the initiation of a left-lateral strike-slip fault east of the bend analogous to the Garlock fault and thrust belts analogous to the Transverse Ranges (Figure 9). However, for intact rock the friction angle is smaller than 45° , and the optimal planes are not perpendicular. With the high friction coefficient that we chose to represent the strength of the intact rock, the angle ψ between σ_1 and the optimal fault strike (in the plane (σ_1, σ_3)) is smaller than for more mature faults with a lower friction coefficient (e.g., 0.6–0.4). Some of the near-fault perturbations, resulting from local stress rotations, can be seen on Figure 9. However, smaller-scale maps would be needed to clearly identify all of them. We chose to point to the largest features that allowed a comparison with actual mapped faults and not to discuss the local perturbations here.

6. Relation Between Fault Strength and Stress Orientations in the Model

[42] We show results from two different times in the model to demonstrate how slip affects the stress rotations: at $t = 3450$ for the lower pore pressure case during phase 2 (section 4) and at $t = 4050$ for the higher pore pressure case

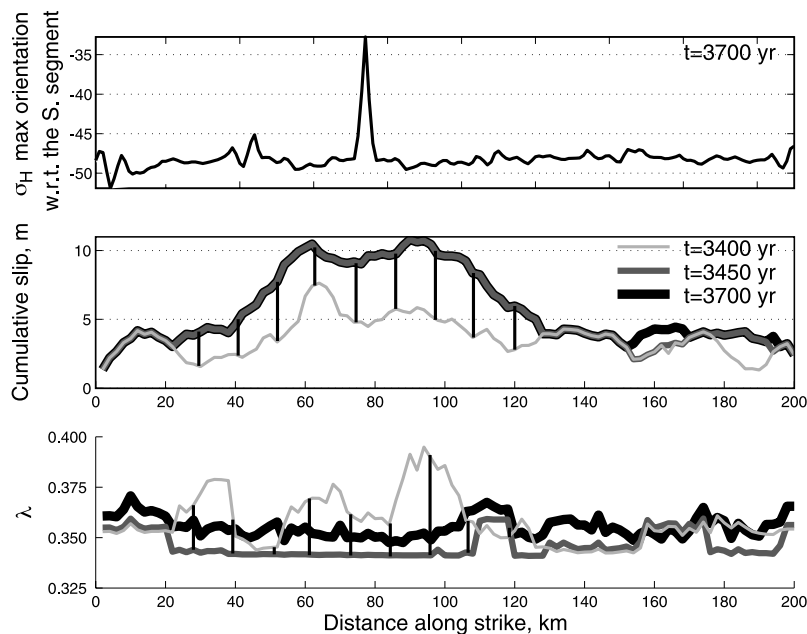


Figure 10. Maximum horizontal stress orientation, cumulative slip and overpressure profiles at 8.5 km depth, at $t = 3400$ (thin light gray line), $t = 3450$ (dark gray line), and $t = 3700$ years (thick black line) on the southern segment (i.e., during phase 2). The hatched region between ~ 20 and 120 km along strike highlights the variations due to a $M_w > 6.9$ event that occurred at $t = 3446$ years. The departures from the average σ_{Hmax} orientation of -50° reflect changes in slope in the cumulative slip profiles and are not correlated with the λ profile. The peak at 80 km is due to a point close to the edge of a dislocation (i.e., singularity).

(phase 3). The areas of stress rotations match the tips of the areas of significantly larger slip as seen on slip profiles calculated at the same depth. These slip profiles show the cumulative slip on each cell. Therefore the stress orientation patterns are not sensitive to the recent seismicity per se but to the relative roughness of the integrated slip history at each location.

[43] We will now investigate the degree of overpressure on the model faults where stress rotations occur and how this might be interpreted in terms of the strength of the faults. As already stated in sections 3.1 and 3.2, pore pressure increases mostly during interseismic periods via pore compaction but also coseismically in the cells adjacent to the slipping cells because of pore pressure redistribution. Pore pressures also decrease during earthquakes both because of frictional dilatancy and to the constant hydraulic head boundary condition at the top of the faults. The degree of overpressure λ can therefore drop significantly when a large rupture initiates at depth, where overpressures are more likely to develop, and propagates to the surface.

6.1. Mostly Strong Fault Case: Phase 2 of the Simulation

[44] When a large portion of the fault is strong (i.e., sustains high shear stress) and the portion with the highest pore pressure fails and ruptures to the surface, the whole λ profile after the event is uniform and at hydrostatic pore pressures. It then takes hundreds of years to build up enough stress to fail this high strength portion of the fault. It appears that stress orientation and cumulative slip are somewhat correlated (see section 5.2) but not that stress is sensitive

only to cumulative slip. It should also be sensitive to loading. In the example of Figure 10, we see that almost no seismic slip occurred between $t = 3450$ and $t = 3700$ years. The stress rotations produced at the time of the earthquake (i.e., at the time of the roughening of the slip profile, see stress concentrations on Figure 11 and stress orientations on Figure 12) can therefore only be modified by the smoothing effect of the large-scale tectonic loading. However, the calculation of the stress changes due to 250 years of plate motion only shows that they are 2 orders of magnitude smaller than the stress tensor values at $t = 3450$ years. It means that if no significant seismicity happens on the fault, there is no way in the model to dissipate the stress perturbations. As will be discussed in section 7.3, postseismic relaxation effects could play a key role in this process and will need to be considered in further studies.

6.2. Weaker Fault Case: Phase 3

[45] When the overpressure profiles show a larger heterogeneity and an overall larger degree of overpressure on the fault, as happens after the onset of ductile compaction, the number of moderate size events increases, smoothing the slip profile so that when large events occur, they create a large anomaly in the slip profile, and large stress rotations ($\pm 50^\circ$) within a 5–10 km radius zone of the tips of the slip “anomaly.” However, this anomaly may not reflect the slip during the last large event for a long time, but rather the low shear stress (stress drop) areas shrinking due to the numerous moderate size earthquakes, as shown by the good correlation between the bumps in the slip profile, i.e., the sudden changes in the slope of the cumulative slip profile

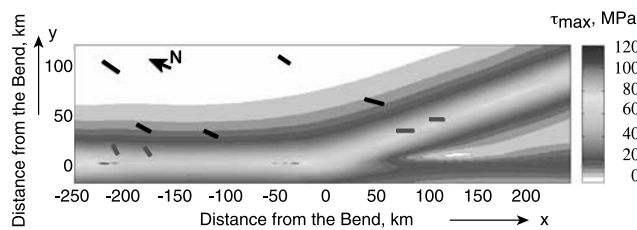


Figure 11. Map of maximum shear stress at 8.5 km depth, at $t = 3450$ years. The black lines show the typical orientation of σ_{Hmax} , whereas thin gray lines show perturbations. The last large earthquake happened at $t = 3446$ years on the southern fault and is responsible for the stress drop around $x = 90$ and 115 km. White corresponds to $\tau_{max} < 10$ MPa.

(Figure 13b), the low maximum shear stress areas on and close to the fault, and the stress orientations (Figure 8) at $t = 4050$ years. The original lateral extension of the large ruptures and the time from these ruptures can both be evaluated by comparing the overpressure profiles at $t = 3950$ years and $t = 4050$ years (Figure 13a). The peak at -30° (also seen on Figure 10) corresponds to only one point, and it results from the proximity of the point where the stress orientation is computed relative to the edge of one of the model fault cells. The reader should therefore not pay attention to the magnitude of the anomaly but rather only note its presence and its sign.

[46] As a conclusion, a testable hypothesis derived from these preliminary results is that stress rotations on mostly strong faults are smaller in magnitude but more persistent in time than those produced by large earthquakes on more overpressured (i.e., weak) faults. This makes sense because ambient deviatoric stresses are high in the “strong fault” case and therefore less readily effected by coseismic stress changes. Besides, in the “strong fault case” the tips of the slip anomaly, and therefore the location of the stress rotations, show the lateral extension of the previous large event and are modified mostly by the next large ($M_w > 6.9$) events, whereas they are expected to change with time because of the intense moderate seismicity on weaker faults.

7. Discussion

7.1. Choice of Model Geometry and Implication for the Strength of the Crust

[47] Section 2 presents the simplest tectonic loading yielding model tectonic domains in accordance with those observed in the Big Bend area. The model North America plate is dragged from its base past the Pacific plate. As expected, the resulting shear stress is localized in the ~ 40 km (twice the depth of the loading dislocation) wide zone overlying the plate boundary. The only source of shear stress far from the plate boundary is due to the far-field compression applied at 400 km from the plate boundary, north of the bend. Therefore, at distances from the plate boundary larger than ~ 40 km the crust in the model is far from being critically stressed, and none of the optimally oriented planes reach failure within the 4000 years of simulations. However surprising, this behavior seems in accordance with some observations. Indeed, both the

Mojave block (northeast of the southern segment) and the central valley (east and northeast of the northern segment) seem to behave as rigid blocks with almost no seismicity. As a reminder, we do not include the East California Shear Zone in our model.

[48] Closer to the plate boundary, however, the optimally oriented planes for failure identified as thrust faults west of the bend and left-lateral strike-slip faults east of it do accumulate shear stresses. On the plate boundary itself the region between the two fault segments accumulates up to 100 MPa of maximum shear stress. Again, despite 4000 years of plate motion and seismicity on the two fault segments, none of these planes reach failure at 8.5 km depth. In these last cases the boundary conditions are yielding high shear stresses, so that the main limitation for the creation of new fractures is the strength of the intact crust.

[49] Because we chose to model two fault segments separated by a locked region with properties of intact (or healed) rock, we could evaluate what it would take to link up the two segments throughout the model bend. Keeping the cohesion value of 20 MPa (already a rather low value compared to the cohesion of intact granite) and the pore pressure in the crust at hydrostatic levels, the friction coefficient assigned to this portion of the crust would need to be as low as 0.3 for a fracture to be created along the plate boundary. This value is far too low to represent a fracture, unless it needs to be seen as an apparent friction coefficient and really means that the pore pressure needs to be much higher.

[50] There are still two alternatives to consider. First, the crust might already host a network of preexisting failure surfaces. Depending on the elapsed time since their last episodes of slip (either seismic or aseismic), their friction and cohesion coefficients could be much lower than for intact rock. Second, we may need to incorporate flaws or other types of weaknesses into the properties of the model crust.

7.2. Stress Orientations, Fault Strength, and Heat Flow

[51] From sections 5.2 and 6, we gather that, first, the average shear stress on the faults is ~ 80 MPa in the stronger case (phase 2, before $t \sim 3800$) and is down to 50–60 MPa at

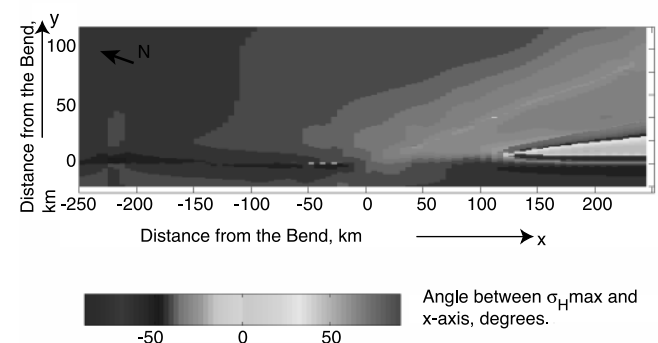


Figure 12. Map of maximum horizontal stress orientation relative to the x axis at 8.5 km depth, at $t = 3450$ years. The last large earthquake happened at $t = 3446$ years on the southern fault and is responsible for the rotations around $x = 90$ and 115 km. See color version of this figure at back of this issue.

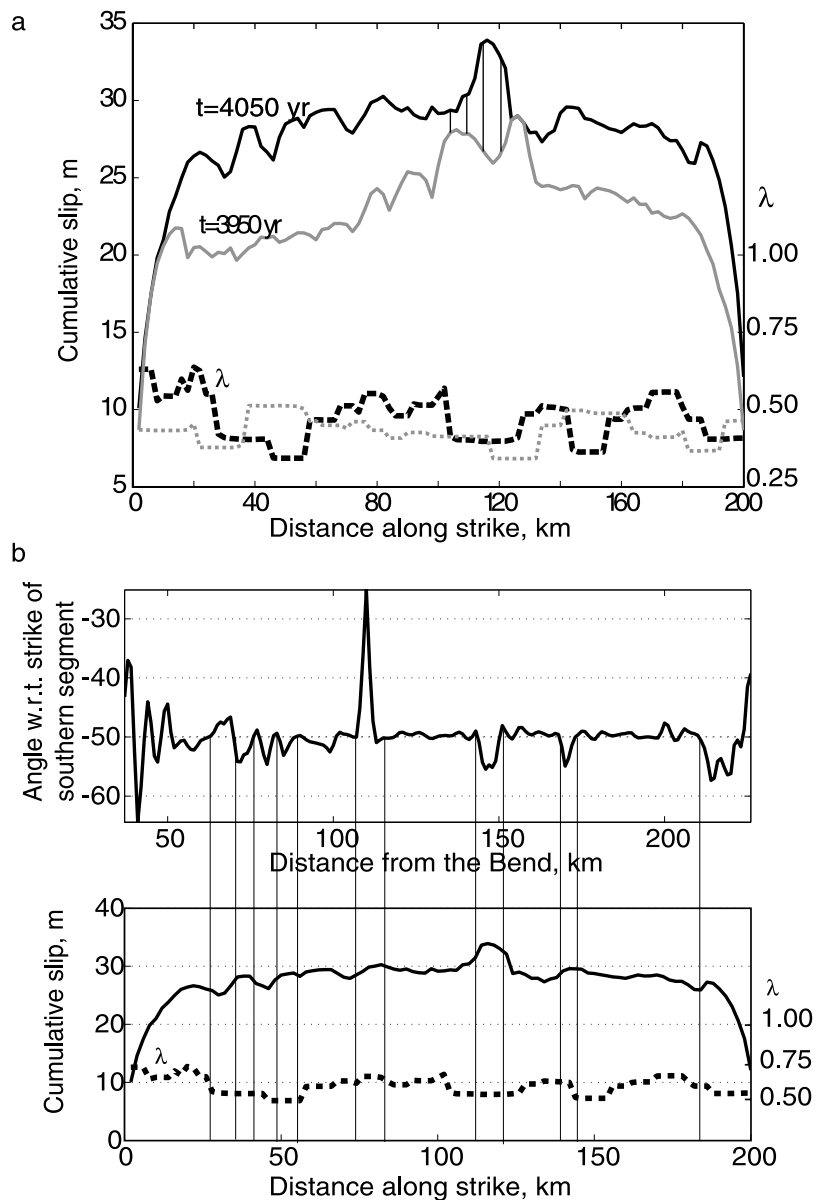


Figure 13. (a) Cumulative slip (solid lines) and overpressure (dotted lines) profiles at 8.5 km depth, at $t = 3950$ and $t = 4050$ years on the southern segment (i.e., during phase 3). The hatched area between ~ 100 and 125 km along strike reflects a $M_w > 6.9$ event that occurred at $t = 4030$ years. (b) Orientation of σ_{Hmax} with respect to the x axis and comparison with the slip and overpressure profiles at $t = 4030$ years. The peak in the orientation profile at 80 km is due to a point close to the edge of a dislocation (i.e., singularity).

the end of the simulation. Second, the average shear stress drop averaged over the whole segment is at least an order of magnitude smaller than the average shear stress, implying that the faults are strong in both phases, according to the definition by *Lachenbruch and Sass* [1992]. For each incremental slip on a subfault the stress drop is fixed to 25% of the preslip stress, but the subfaults are reloaded by stress transfer from slip on other subfaults and can also slip several times during the same event, so that the static stress drop cannot be determined by model assumptions. Third, the maximum horizontal stress orientations at midcrustal depth are shown to rotate (smoothly) to a lower angle between 40 and 60° to the fault strike in most of the region within 20 km of the model faults. Noticeable exceptions are close to the

tips of the faults (at the transition between active fault and intact rock), where the orientations can rotate to almost perpendicular to the faults, and close to the tips of a low in shear stress on the model faults, where the orientation can become even more fault parallel. The stress orientations therefore exhibit “middle angles” that can be interpreted as indicative of strong faults [Scholz, 2000] or not [Townend and Zoback, 2001]. Another observation is that the degree of overpressure, when averaged over the fault plane, is lower than 0.6 at all times during the simulation, which might not be considered a severe overpressure. However, it is locally as high as 0.75 at depths lower than 6 km. All the usual criteria that could be evaluated with measurable properties are therefore inconclusive.

[52] The ultimate test of fault strength is often considered to be the heat flow anomaly measured at the surface and due to heat production from frictional fault slip at depth. The time constant for heat conduction is very large (e.g., millions of years). The heat flow measured in one point at the surface therefore accounts for the integrated effects of all the seismicity that occurred in the volume of rock defined by depth times total lateral offset during millions of years. In order to interpret the results in terms of fault strength it is usually assumed that the fault is at a steady state. Because geodetic and paleoseismology can give estimates of the average fault slip rate during these periods, one can then infer an estimate of the time and spatial average of frictional strength during the rupture propagation by comparing calculated values for different shear strength depth profiles to actual measurements. *Lachenbruch and Sass* [1992] show that for an average frictional stress of 100 MPa (strong fault case) and a slip rate of 30 mm yr^{-1} , the average heat production would be 100 mW m^{-2} , and the heat flow anomaly after a few million years would equal the background heat flow, which is much greater than what was measured across the San Andreas fault.

[53] A natural test for our model would be to calculate the heat flow at the surface due to the model seismicity. However, by nature, our model presents transient features rather than a steady state behavior. Because we studied a restricted area in the San Andreas fault system during a limited amount of time (~ 4000 years), the two short model fault segments (200 km long) should be considered as the initial faults within an evolving system. The finiteness of the segments precludes the average fault slip rate to be equal to plate velocity within this time window and also guarantees that stresses will accumulate near the tips of the segments and will fail the brittle crust into new faults. During the 350 years of the weaker phase the average shear stress on the southern segment is 60 MPa, and the average slip rate is 12 mm yr^{-1} . The heat flow due to frictional slip on the southern segment is therefore on the order of 20 mW m^{-2} assuming the shear strength during failure equals the shear stress. If this situation were to last for a million years or so (which is not likely), this result would still be consistent with heat flow measurements across the San Andreas [*Lachenbruch and Sass*, 1992]. However, in the last hundred years of the simulation the slip rate is, in fact, larger than the average plate velocity. The system had accumulated lots of slip deficit during phases 1 and 2 (difference between plate motion and fault slip) and release it in phase 3 because the faults are weakening.

[54] An alternative to this “fault physics based self-building fault system” method is the choice of much longer faults with a simplified physics studied within the framework of long-term crustal deformation models. These models assume uniform fault properties along strike and use present-day GPS measurements to constrain the kinematic boundary conditions. They test for friction coefficients of the fault and for the viscoelastic structure of the lower crust and/or upper mantle to match measured stress orientations and heat flow [*Lynch and Richards*, 2001; *Chéry et al.*, 2001]. Once the initial conditions (unstressed viscoelastic material) no longer influence the model behavior (after 6000 years in the case of *Lynch and Richards* [2001]), they compute constant average fault slip rates. They either look at the model behavior on a cross section at the center of the fault to

avoid edge effects that they consider as errors [*Lynch and Richards*, 2001] or consider that the plane perpendicular to the fault strike is a symmetry plane, implying that the fault is “infinite” [*Chéry et al.*, 2001]. In the latter case, *Chéry et al.* acknowledge that other faults may form progressively in the surrounding crust, and they add a strain-softening term to account for the decrease of the crustal strength due to these faults.

7.2.1. Comment on Frictional Strength Evaluation

[55] The elastic loading at the base of the model causes much greater shear stresses at depth than in the shallower parts of the fault in a way that can not be approximated by a linear trend for the whole depth range. The shear stress averaged over the southern segment is ~ 60 MPa (Figure 5) but varies a lot along strike between 50 and 70 MPa and in depth (e.g., ~ 30 MPa at 5 km depth, ~ 50 MPa at 10 km, and ~ 150 MPa at 18 km depth). *Lachenbruch and Sass* [1980] showed that the heat anomaly measured above a fault with mostly deep slip was not only slower to appear but also smaller in amplitude. It is recorded at the end of a time step, i.e., after the arrest of an event on one of the fault segments, and does not reflect the dynamic shear stress acting during the ruptures but rather the static shear stress sustained by the fault segments. In the model the imposed reduction in friction on a cell from static to dynamic once it slipped is very simple, but the effective evolution of the strength of a cell throughout the “quasi-static” propagation is very complex. *Miller* [2002] showed the pseudodynamic weakening behavior due to stress transfer. Another aspect is related to the pore pressure redistribution scheme of the present model. Contrary to *Miller* [2002], pore pressures are redistributed only once the fault is stable with respect to its stress state. This can result in pore pressures being equilibrated within a patch of the fault that previously had a very different pore pressure. In this case, the strength of the previously low-pressure (often shallower) cells would drop dramatically, leading to the further propagation of the rupture but at a lower (dynamic) stress level. The nonlinear stress profile, added to the likely weakening of the fault during rupture just discussed, would lead to an heat flow anomaly more difficult to detect than the generic case. In the extreme case when the rupture reaches the constant hydraulic head boundary condition at the top of the fault, resulting in outflow, the fluid flow would probably perturb the heat signal caused by the earthquake.

7.2.2. Model Fault Slip Rate

[56] The other ingredient for heat flow calculations is the fault slip rate. It is also very heterogeneous, both spatially and in time. Averaged over the last 350 years, slip rate on the southern segment is $\sim 12 \text{ mm yr}^{-1}$, ranging between 4 and 17 mm yr^{-1} along strike. Over the last 100 years it is more than 3 times higher, both because of the previously stored slip deficit and the lower strength of the fault and the subsequent denser occurrence of small-sized earthquakes. The expected next steps in the evolution of the modeled fault system is the breaking of the bend and of new faults near the tips of the prescribed faults, which would release both shear stresses in the yet unbroken regions and the pore pressure in the present faults. The longer the fault becomes, the more the slip rate is likely to increase. However, it is difficult to describe what a steady state would be in such an evolving fault system, where new faults are likely to be

created and other segments likely to be abandoned. As a conclusion, a proper calculation of heat flow would be an integration over time of all incremental elements (strength times slip) for each depth during each earthquake for simulations of hundreds of thousands or millions of years. This is beyond the scope of the present study.

7.3. Postseismic Relaxation

[57] In section 5.2 we investigated the time extent of the perturbations in the stress orientations. One process that we did not include is the smoothing of the stress state due to postseismic relaxation. In a preliminary study of the influence of postseismic relaxation for the same Big Bend setting, *Fitzenz et al.* [2002] added a viscoelastic half-space below the seismogenic layer and calculated the toroidal component of the relaxation due to the $M_w > 6$ events only (to save computational time). They integrated this effect into the forward model by linearizing the sum of the stressing rates because of all past relevant earthquakes at a given time, to be able to keep the quasi-static approach and to calculate the exact time step to the next rupture. They show that some 15 years after the first large earthquake, the average properties on the faults and the frequency-size statistics start departing significantly from the no relaxation case.

8. Conclusion

[58] Our aim was to distinguish the large-scale stress patterns (or tectonic regimes) resulting from the boundary conditions alone from those due to fault slip and to identify measurable stress indicators of the state of the faults both for a stronger fault case and weaker case. Because we studied a restricted area in the San Andreas fault system during a limited amount of time (~ 4000 years), the two short model fault segments should be considered as the initial faults within an evolving system. We designed a forward regional model of the southern San Andreas fault system near the Big Bend that includes tectonic loading, fault zone hydraulics, and stress transfer. The prescribed fault system is made of two 200 km long strike-slip fault segments oriented at 20° of each other separated by a region that has the properties of intact rock (e.g., lithified fault segment). The introduction of ductile compaction and shear creep after the first large ruptures on the two active fault segments induced a rapid increase in pore pressure and led to fault weakening, allowing for the study of both mostly strong faults (before ductile compaction and shear creep) and weaker faults (after their introduction).

[59] The stress orientations close to the model fault exhibit middle angles ($40\text{--}50^\circ$) relative to the fault strikes, consistent with results from *Hardebeck and Hauksson* [2001] and *Townend and Zoback* [2001] and are at a higher angle far (distances greater than 70 km) from the faults, especially in the area northeast of the bend where the far-field compression is the dominant source of deviatoric stress. The orientation of the maximum horizontal stress in this far-field area (east of the northern segment) is expected to rotate clockwise with time to reach values comparable to that observed ($\sim 70^\circ$ relative to the strike of the northern segment, i.e., x axis), especially if the San Andreas fault was modeled as a continuous fault across the bend.

[60] Significant local rotations are observed because of fault slip. They are localized in a narrow zone centered on

the fault ($\pm 5\text{--}10$ km), where the cumulative slip departs from the average slip on the profile at the depth of the calculation. They are not persistent with time, unless the faults are very strong, and it takes a long time to again smooth the slip profile. These migrations of the stress rotations could be tested in nature.

[61] In the longer-term and at a larger scale the 4000 years of seismicity on the model faults incrementally changes the stress state in the model region, so that the areas in transpressive regimes tend to migrate north toward the bend (something plate motion alone could not trigger in 100,000 years, see section 2).

[62] We decided to separate the northern and the southern segment by intact rock for mathematical convenience. Although not appropriate for the geology of the San Andreas fault at this location, it allowed us to test in a generic way what it would take to link up two fault segments. An intriguing conclusion of this study is that it is very hard to break intact rock. Indeed, even the region on the plate boundary between the two fault segments does not break within the 4000 years of the simulation despite a high shear stress concentration. Pockets of high pore pressure, preexisting fractures, and material weaknesses all could lower the failure criterion. Their occurrence (or not) in the crust surrounding the plate boundary in southern California near the bend needs to be further investigated. The many faults mapped close to the San Andreas in other areas certainly point to the importance of preexisting weaknesses (e.g., the flower structures identified close to the San Andreas fault near Parkfield [*Rymer et al.*, 2003]).

[63] However, the main question one can ask after such a study is: Are the model faults weak or strong? The magnitude of shear stress and the ratio of stress drop to shear stress tend to point to strong faults, while stress orientations (middle angle) do not allow a conclusion. Finally, the distribution of pore pressure, in particular below 6 km depth, would definitely point to a strong fault during phase 2 and a weak fault during phase 3. Unfortunately, pore pressures are very difficult to infer and impossible to measure at these depths. A last argument to distinguish between weak and strong is usually the heat flow argument. Strong faults are purported to produce a large heat flow anomaly due to frictional sliding. In the model the average fault slip rate is very time dependent, and is about half the plate velocity over the last 350 years, because of the fact that the faults are finite. Together with a static shear stress on the order of 50 MPa, the estimated average heat flow is on the order of 20 mW m^{-2} and varies along strike. Since the fault system did not reach a steady state, this heat flow estimation cannot be extrapolated to time periods long enough to compare with the time constant for heat conduction, and no conclusion can be drawn this way regarding the strength of the fault segments.

[64] Since individual faults in real fault systems, such as the San Andreas fault system in the San Francisco Bay area, can exhibit very variable slip rates with time (e.g., constant slip rates for less than 2 million years on some faults [*Wakabayashi*, 1999]), it is important to identify criteria to evaluate fault strength, other than heat flow.

[65] In our model the two fault segments do exhibit different behaviors from phase 2 to phase 3, differences which could be very important, were we to assess the seismic

hazard they represent. Unless boreholes can be drilled through the faults at seismogenic depths and pore pressure, stresses, and heat flow can be measured in the fault zone itself; only two sets of observable parameters distinguish the two phases in this study. They are (1) the increase in the number of small to medium-sized earthquakes in the fault weakening phase and (2) the rotations of the maximum horizontal stress close to the fault following a large event, and how they persist and how their location changes with time. The former could be evidenced by changes in b values, whereas the latter could be seen on focal mechanism inversions, provided enough earthquakes happen to see a time evolution in the resulting stress orientations.

[66] Changes in the seismicity (e.g., number of events per time window, size of events) were also shown to be a proxy for the stress state on faults for constant strength numerical models [Ben-Zion *et al.*, 2003]. In that study, they were used to identify periods during which large (system-sized) earthquakes could happen. In a future work, it would be interesting to compare the statistics of this model to similar ones computed from our simulation for phases 2 and 3, using the more complex strength model (where the strength of the fault segments is highly variable in time and spatially heterogeneous).

[67] These preliminary modeling results demonstrate the potential utility of regional fault models for investigating some fundamental issues in fault mechanics and regional tectonics. In particular, they enable a treatment of the three dimensionality of fault systems and permit the test of theories developed for 1-D models or homogeneous faults infinite along strike. Although the results of the regional model presented here demonstrate that the model and its boundary conditions have most of the ingredients to produce a realistic numerical analog to the SAF, additional studies are necessary.

[68] Specifically, the questions of (1) the initial shear stress in the crust, (2) the continuity of the model faults across the bend, (3) the existence or not of steady state behavior in natural fault systems, (4) the dynamic weakening, and (5) the importance of postseismic relaxation need to be addressed. In addition, the behavior of the model faults is strongly influenced by (1) their pore pressure, so additional studies are needed to better constrain flow in and around fault zones and mechanisms of porosity reduction and (2) the length of the active part of the fault, pointing to the need for the modeling of fault strengthening and lithification.

Appendix A: Interseismic Permeabilities

[69] The interseismic in-plane permeabilities are calculated from the relationship [Brace, 1978]:

$$k = k_o \phi^3, \quad (\text{A1})$$

where k is the permeability, ϕ is the porosity, and k_o is proportional to the hydraulic radius. We keep k_o very small and constant during interseismic periods, that is, from right after a rupture to the onset of the next event. This assumption is questionable since the sealing of the hydraulic paths created during faulting probably takes time, but this is beyond the scope of the present study. Faulkner and Rutter [2001] measured fault gouge permeabilities of

$\sim 10^{-18} \text{ m}^2$ in a direction parallel to the fault plane in the Carboneras (Spain) strike-slip fault. They also measured an in-plane anisotropy, with vertical permeability (k_z) more than 1 order of magnitude higher than the horizontal permeability (k_x). Rawling *et al.* [2001] review fault gouge permeabilities from $\sim 10^{-20} \text{ m}^2$ to $\sim 10^{-19} \text{ m}^2$. Assuming that in-plane permeability is anisotropic and a cubic function of porosity, we get $k_x = k_{ox} \phi^3$ and $k_z = k_{oz} \phi^3$, with $k_{ox} = 10^{-15} \text{ m}^2 < k_{oz} = 10^{-13} \text{ m}^2$.

Appendix B: Interseismic Compaction and Shear Creep

[70] The total interseismic pore pressure change rate is given by the sum of a positive compaction term corrected to give smaller pore pressure increases as the porosity decreases to values close to the minimum porosity and a negative leakage term:

$$\frac{\partial P_f}{\partial t} = - \frac{(P_f - \sigma_n)}{\beta_f \phi} \frac{2}{\eta_i} \left[\frac{13 + 4\phi}{63 + 36\phi} \right] \left[\frac{\phi - \phi_{\min}}{\phi_{\max} - \phi_{\min}} \right]^a - \frac{P_f - P_h}{t_h}, \quad (\text{B1})$$

where P_f is pore pressure and σ_n is normal stress within the fault core, η_i is the intrinsic viscosity of the grains (i.e., the deformation of individual grains is time-dependent), P_h is the hydrostatic pore pressure of the surrounding rocks, and t_h is the out-of-plane diffusion time. For simplicity, we keep the maximum porosity constant $\phi_{\max} = 9\%$ and the residual porosity $\phi_{\min} = 2\%$. The exponent a controls the rapidity of the falloff of the compaction rate when ϕ becomes close to ϕ_{\min} . The shear creep velocity V is a function of the fault core width W , the driving shear stress, and the viscosity of the fault zone. The latter is expressed as a function of porosity and the intrinsic viscosity of the grains, resulting in

$$V = \tau W \frac{13 + 4\phi}{9\eta_i}, \quad W = W_0 + \epsilon D. \quad (\text{B2})$$

Note that V is the velocity of one wall of the fault zone with respect to the other wall and that W evolves as a function of cumulative slip D (ϵ is a constant) from an initial width W_0 . For computational convenience, we update stress transfer from creep slip using Okada's [1985] analytical solutions every 50 years. Where not otherwise specified, the model parameters are given in Table 3.1 of Fitzenz and Miller [2003].

Appendix C: Optimal Orientation for Faulting in the General Case of a 3-D Stress Tensor

[71] First, if the three principal stresses σ_1 , σ_2 and σ_3 are distinct, for a given unit normal \vec{n} to a plane Π , the normal (σ) and shear (τ) stresses acting on Π satisfy:

$$\begin{aligned} \sigma_1 n_1^2 + \sigma_2 n_2^2 + \sigma_3 n_3^2 &= \sigma, \\ \sigma_1^2 n_1^2 + \sigma_2^2 n_2^2 + \sigma_3^2 n_3^2 &= \sigma^2 + \tau^2, \\ n_1^2 + n_2^2 + n_3^2 &= 1. \end{aligned} \quad (\text{C1})$$

Solving for (n_1, n_2, n_3) this Vandermonde equation system, we get for distinct principal stresses:

$$n_1^2 = \frac{(\sigma_3 - \sigma)(\sigma_2 - \sigma) + \tau^2}{(\sigma_1 - \sigma_3)(\sigma_1 - \sigma_2)}, \quad (C2)$$

and n_2^2 and n_3^2 can be obtained similarly by circular permutation. Therefore the equations $n_i = \text{const}$, $i = 1, 2, 3$, define three families of circles, the circle $n_2 = 0$ being the locus of the maximum shear stress (circle with ordinate intercepts at σ_3 and σ_1). This is equivalent to saying that the principal stress direction associated with σ_2 belongs to the optimal fault plane (for a maximum shear stress).

[72] Second, the optimal angle between σ_1 and the strike of the fault plane in the plane defined by (σ_1, σ_3) is calculated by maximizing the Coulomb failure stress and is given by $\psi = \frac{1}{2} \tan^{-1}(-1/\mu)$, where μ is the friction coefficient (for the details of this calculation in the 2-D case, see King *et al.* [1994]). This defines a second vector lying in the fault plane, and together the two vectors enable the calculation of both strike and dip angles of the optimal plane. Since $+\psi$ and $-\psi$ are equally valid, a given principal stress tensor yields two sets of strike and dip angles at each location. We can calculate the new absolute Coulomb failure stress on these planes and check if new failure planes would be created. This method is different from the usual hypothesis in Δ CFS studies [e.g., King *et al.*, 1994; Stein *et al.*, 1997], where faults of all orientations are assumed to already exist and where the ψ angle is used as a fitting parameter to fit areas of increased CFS to aftershock locations.

[73] **Acknowledgments.** The authors want to thank Fred Pollitz, Bob Simpson, Jim Savage, and Colin Williams for insightful discussions and the internal review crew for their useful comments on the manuscript. Thanks also to two anonymous reviewers, Susan Ellis, and Joan Gombert for their comments and suggestions. This research was partially supported by the Swiss National Fund, program 2100-054121.98/1 and by a Swiss National Fund post-doc fellowship.

References

- Andrews, D. J. (2002), A fault constitutive relation accounting for thermal pressurization of pore fluid, *J. Geophys. Res.*, *107*(B12), 2363, doi:10.1029/2002JB001942.
- Argus, D. F., and R. G. Gordon (1991), Current Sierra Nevada-North America motion from very long baseline interferometry: Implications for the kinematics of the western United States, *Geology*, *19*, 1085–1088.
- Ben-Zion, Y., M. Eneva, and Y. Liu (2003), Large earthquake cycles and intermittent criticality on heterogeneous faults due to evolving stress and seismicity, *J. Geophys. Res.*, *108*(B6), 2307, doi:10.1029/2002JB002121.
- Brace, W. (1978), A note on permeability changes in geologic material due to stress, *Pure Appl. Geoph.*, *116*, 627–633.
- Bretoner, R., and B. Muller (1991), European stress—Contributions from borehole breakouts, *Philos. Trans. R. Soc. London, Ser. A*, *337*, 165–179.
- Chéry, J., M. D. Zoback, and R. Hassani (2001), An integrated mechanical model of the San Andreas fault in central and northern California, *J. Geophys. Res.*, *106*, 22,051–22,066.
- Faulkner, D. R., and E. H. Rutter (2001), Can the maintenance of overpressured fluids in large strike-slip fault zones explain their apparent weakness?, *Geology*, *29*, 503–506.
- Fitzenz, D. D., and S. A. Miller (2001), A forward model for earthquake generation on interacting faults including tectonics, fluids, and stress transfer, *J. Geophys. Res.*, *106*, 26,689–26,706.
- Fitzenz, D. D., and S. A. Miller (2003), Fault compaction and overpressured faults: Results from a 3D model of a ductile fault zone, *Geophys. J. Int.*, *155*, 111–125.
- Fitzenz, D. D., F. Pollitz, and S. A. Miller (2002), First results of a physics-based, integrative model of the San Andreas fault system near the Big Bend including fluids, tectonics, and post-seismic relaxation, *Eos Trans. AGU, Fall Meet. Suppl.*, Abstract T71D-1191.
- Gratier, J.-P., P. Favreau, and F. Renard (2003), Modeling fluid transfer along California faults when integrating pressure solution crack sealing and compaction processes, *J. Geophys. Res.*, *108*(B2), 2104, doi:10.1029/2001JB000380.
- Guéguen, Y. and V. Palciauskas (Eds.) (1992), *Introduction à la Physique des Roches*, Hermann, Paris.
- Hardebeck, J. L., and E. Hauksson (1999), Role of fluids in faulting inferred from stress field signatures, *Science*, *285*, 236–239.
- Hardebeck, J. L., and E. Hauksson (2001), Crustal stress field in southern California and its implications for fault mechanics, *J. Geophys. Res.*, *106*, 21,859–21,882.
- Hubbert, M. K., and W. W. Rubey (1959), Role of fluid pressure in mechanics of overthrust faulting, *Geol. Soc. Am. Bull.*, *70*, 115–166.
- Ikeda, R., Y. Iio, and K. Omura (2001), In situ stress measurements in NIED boreholes in and around the fault zone near the 1995 Hyogo-ken Nambu earthquake, Japan, *Island Arc*, *10*, 252–260.
- King, G. C. P., R. S. Stein, and J. Lin (1994), Static stress changes and the triggering of earthquakes, *Bull. Seismol. Soc. Am.*, *84*, 935–953.
- Lachenbruch, A. H., and J. H. Sass (1980), Heat flow and energetics of the San Andreas fault zone, *J. Geophys. Res.*, *85*, 6185–6222.
- Lachenbruch, A. H., and J. H. Sass (1992), Heat flow from Cajon Pass, fault strength, and tectonic implications, *J. Geophys. Res.*, *97*, 4995–5015.
- Lockner, D. A., and N. Beeler (2003), Stress-induced anisotropic poroelasticity response in sandstone, paper presented at ASCE Conference, Am. Soc. of Civ. Eng., Seattle, Wash.
- Lynch, J., and M. Richards (2001), Finite element models of stress orientations in well-developed strike-slip fault zones: Implications for the distribution of lower crustal strains, *J. Geophys. Res.*, *106*, 26,689–26,706.
- Michael, A. (1987), The use of focal mechanisms to determine stress: A control study, *J. Geophys. Res.*, *92*, 357–368.
- Miller, S. A. (2002), Properties of large ruptures and the dynamical influence of fluids on earthquakes and faulting, *J. Geophys. Res.*, *107*(B9), 2182, doi:10.1029/2000JB000032.
- Miller, S. A., A. Nur, and D. L. Olgaard (1996), Earthquakes as a coupled shear stress-high pore pressure dynamical system, *Geophys. Res. Lett.*, *23*, 197–200.
- Miller, S. A., Y. Ben-Zion, and J.-P. Burg (1999), A three dimensional fluid-controlled earthquake model: Behavior and implications, *J. Geophys. Res.*, *104*, 10,621–10,638.
- Morrow, C., D. A. Lockner, S. Hickman, M. Rusanov, and T. Rockel (1994), Effects of lithology and depth on the permeability of core samples from the kola and ktb drillholes, *J. Geophys. Res.*, *99*, 7274–7623.
- Nur, A., and J. D. Byerlee (1971), An exact effective stress law for elastic deformation of rock with fluids, *J. Geophys. Res.*, *76*, 6414–6419.
- Okada, Y. (1985), Surface deformation due to shear and tensile faults in a half-space, *Bull. Seismol. Soc. Am.*, *75*, 1135–1154.
- Prescott, W. H., J. Savage, J. L. Svarc, and D. Manaker (2001), Deformation across the Pacific-North America plate boundary near San Francisco, California, *J. Geophys. Res.*, *106*, 6673–6682.
- Provost, A., and H. Houston (2001), Orientation of the stress field surrounding the creeping section of the san andreas fault: Evidence for a narrow mechanically weak fault zone, *J. Geophys. Res.*, *106*, 11,373–11,386.
- Rawling, G. C., L. B. Goodwin, and J. L. Wilson (2001), Internal architecture, permeability structure, and hydrologic significance of contrasting fault-zone types, *Geology*, *29*, 43–46.
- Rice, J. R. (1992), Fault stress states, pore pressure distributions, and the weakness of the San Andreas fault, in *Fault Mechanics and Transport Properties of Rocks*, *Int. Geophys. Ser.*, edited by B. Evans and T.-F. Wong, pp. 9885–9907, Academic, San Diego, Calif.
- Rymer, M., M. R. Catchings, and M. Goldman (2003), Structure of the San Andreas fault zone as revealed by surface geologic mapping and high-resolution seismic profiling near Parkfield, California, paper presented at European Geophysical Society-American Geophysical Union-European Union of Geophysicists Joint Assembly, Nice, France.
- Scholz, C. H. (2000), Evidence for a strong San Andreas fault, *Geology*, *28*, 163–166.
- Sibson, R. H. (1992), Fault-valve behavior and the hydrostatic-lithostatic fluid pressure interface, *Earth Sci. Rev.*, *32*, 141–144.
- Simpson, R. W. (1997), Quantifying Anderson's fault types, *J. Geophys. Res.*, *102*, 17,909–17,919.
- Sleep, N. (1995), Ductile creep, compaction and rate and state dependent friction within major fault zones, *J. Geophys. Res.*, *100*, 13,065–13,080.
- Sleep, N., and M. L. Blanpied (1992), Creep, compaction and the weak rheology of major faults, *Nature*, *359*, 687–692.

- Stein, R. S., A. A. Barka, and J. H. Dieterich (1997), Progressive failure on the North Anatolian fault since 1939 by earthquake stress triggering, *Geophys. J. Int.*, *128*, 594–604.
- Talwani, P., J. S. Cobb, and M. F. Schaeffer (1999), In situ measurements of hydraulic properties of a shear zone in northwestern South Carolina, *J. Geophys. Res.*, *104*, 14,993–15,003.
- Terzaghi, K. (1923), Die berechnung der durchlässigkeitsziffer des tones aus dem verlauf der hydrodynamischen spannungserscheinungen, *Adad. Wiss. Wien*, *132*, 125–138.
- Townend, J., and M. D. Zoback (2000), How faulting keep the crust strong, *Geology*, *28*, 399–402.
- Townend, J., and M. D. Zoback (2001), Implications of earthquake focal mechanisms for the frictional strength of the san andreas fault system, in *The Nature and Tectonic Significance of Fault Zone Weakening*, edited by R. E. Holdsworth et al., *Geol. Soc. Spec. Publ.*, *186*, 13–21.
- Tsukahara, H., R. Ikeda, and K. Omura (1996), In-situ stress measurement in an earthquake focal area, *Tectonophysics*, *262*, 281–290.
- Wakabayashi, J. (1999), Distribution of displacement on and evolution of a young transform fault system: The northern San Andreas fault system, California, *Tectonics*, *18*, 1245–1274.
- Zhu, L., and D. Helmberger (1996), Advancements in source estimation techniques using broadband regional seismograms, *Bull. Seismol. Soc. Am.*, *86*, 1634–1641.
- Zoback, M. D., and J. H. Healy (1992), In situ stress measurements to 3.5 km depth in the Cajon Pass scientific research borehole: Implications for the mechanics of crustal faulting, *J. Geophys. Res.*, *97*, 5039–5057.

D. D. Fitzenz, U.S. Geological Survey MS-977, 345 Middlefield Road, Menlo Park, CA 94025, USA. (fitzenz@usgs.gov)

S. A. Miller, Institute of Geophysics, Swiss Federal Institute of Technology, ETH Hônggerberg, CH-8093 Zürich, Switzerland.

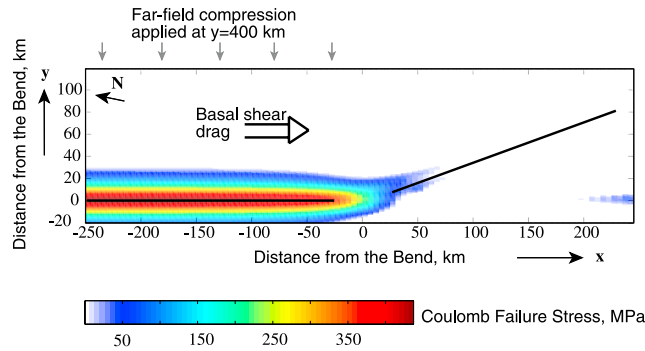


Figure 3. Map of Coulomb failure stress (CFS) calculated at 8.5 km depth due to 100,000 years of tectonic loading. The two modeled fault segments of the San Andreas fault (black lines) are shown to be the first faults to accumulate enough stresses to reach the failure criterion. The southern segment accumulates less CFS because of the high normal stresses. White corresponds to $CFS \ll 15$ MPa.

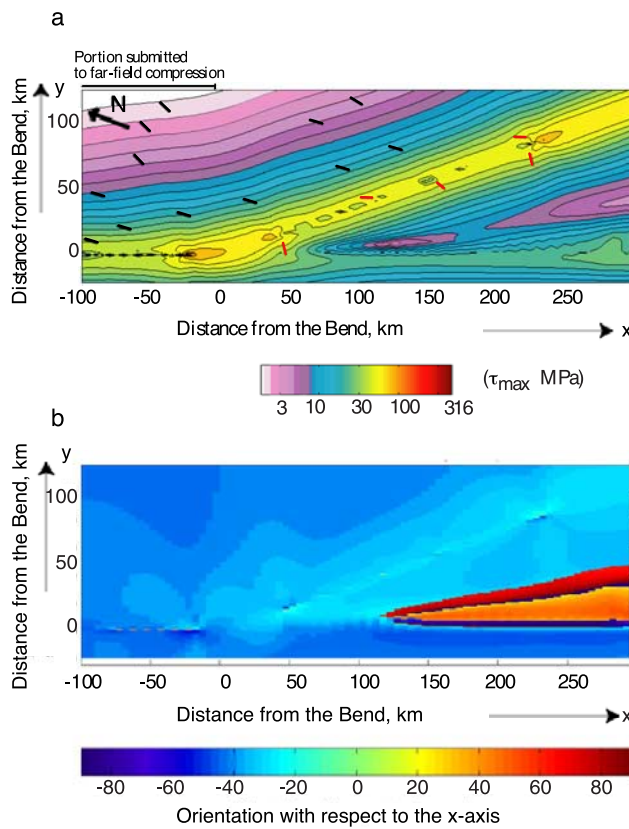


Figure 8. (a) Maximum shear stress (colors) and σ_{Hmax} orientations (characteristic trends, white lines, and local perturbations, red lines) and (b) orientation of σ_{Hmax} relative to x axis. Both maps are calculated at 8.5 km depth. τ_{max} is maximum in a 40 km wide zone (~ 70 MPa) centered at the plate boundary and is largely perturbed near the faults (e.g., stress drops and stress transfer). The term σ_1 is consistently oriented $\sim 45^\circ$ to the northern segment, and $\sim 55^\circ$ to the southern segment in a 20 km wide band. However, it locally rotates to be either almost perpendicular or subparallel to the fault strike.

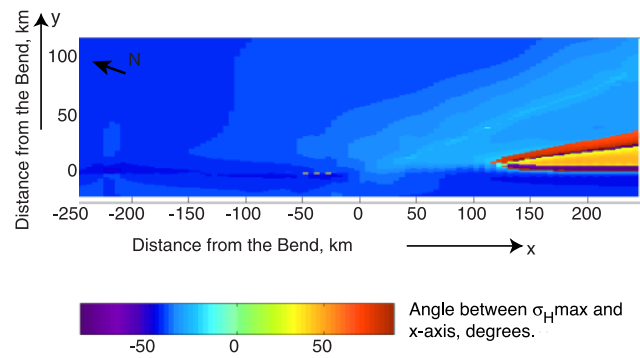


Figure 12. Map of maximum horizontal stress orientation relative to the x axis at 8.5 km depth, at $t = 3450$ years. The last large earthquake happened at $t = 3446$ years on the southern fault and is responsible for the rotations around $x = 90$ and 115 km.